



Collective self-optimization of binary mixed heterogeneous populationsZhao-sha Tang,¹ Jia-jian Li ¹, Wei-jing Zhu,² and Bao-quan Ai ^{1,3,*}¹*Key Laboratory of Atomic and Subatomic Structure and Quantum Control (Ministry of Education), Guangdong Basic Research Center of Excellence for Structure and Fundamental Interactions of Matter, School of Physics, South China Normal University, Guangzhou 510006, China*²*School of Photoelectric Engineering, Guangdong Polytechnic Normal University, Guangzhou 510665, China*³*Guangdong Provincial Key Laboratory of Quantum Engineering and Quantum Materials, and Guangdong-Hong Kong Joint Laboratory of Quantum Matter, South China Normal University, Guangzhou 510006, China*

(Received 1 June 2023; accepted 16 January 2024; published 14 February 2024)

To maximize the survival chances of society members, collective self-organization must balance individual interests with promoting the collective welfare. Although situations where group members have equal optimal values are clear, how varying optimal values impacts group dynamics remains unclear. To address this gap, we conducted a self-optimization study of a binary system incorporating communication-enabled active particles with distinct optimal values. We demonstrate that similar particles will spontaneously aggregate and separate from each other to maximize their individual benefits during the process of self-optimization. Our research shows that both types of particles can produce the optimal field values at low density. However, only one type of particle can achieve the optimal field values at medium density. At high densities, neither type of particle is effective in reaching the optimal field values. Interestingly, we observed that during the self-optimization process, the mixture demixed spontaneously under certain circumstances of mixed particles. Particles with higher optimal values developed into larger clusters, while particles with lower optimal values migrated outside of these clusters, resulting in the separation of the mixture. To achieve this separation, suitable noise intensity, particle density, and the significant difference in optimal values were necessary. Our results provide a more profound comprehension of the self-optimization of synthetic or biological agents' communication and provide valuable insight into separating binary species and mixtures.

DOI: [10.1103/PhysRevE.109.024405](https://doi.org/10.1103/PhysRevE.109.024405)**I. INTRODUCTION**

Numerous systems in both technological and natural realms comprise a mixture of diverse particle types. The combination and subsequent separation of each particle type yield phenomenology that is extraordinarily rich in comparison with monodisperse systems. The separation of particles is one of the fundamental challenges related to binary mixtures of particles. Binary mixtures [1–20], made up of different particles, might demix if their constituents have distinct properties, such as mass, size, motility, chirality, and so on. Phase separation (mixed particle separation) is of great importance in physics as it allows us to study the behavior and properties of different phases (components) within a system, leading to a better understanding of phenomena like phase transitions, critical phenomena, and the formation of complex structures in materials.

Particle systems capable of intercommunication have garnered substantial interest. Communication is vital for survival and offers an evolutionary edge to communicating organisms [21,22]. Chemotaxis, which cells have developed as a simple yet efficient adaptive mechanism, is another striking

example [23–28]. Numerous examples of communication in active matter emerge from nature [29–31], including protein waves facilitating cargo transport [32], auditory cues helping insects create cohesive groups [33], and microrobots and soft robotic fish utilizing infrared, electric, and sound signals for communication [34–37]. Further, animal huddling for warmth, observed in birds [38], mice [39], and notably penguins [40,41], demonstrates another instance of natural communication. When the active particles with chemotactic properties are composed of multiple components, the mixing characteristics of these particles significantly influence the system's dynamic properties.

The chemotactic autoaggregation phenomenon [42,43] has been modeled in numerous ways, such as the classic Patlak-Keller-Segel model [44–48]. These models take into account the volume limits caused by the presence of cells in a certain area. Such limits can restrict space and block other cells from invading the area. In a recent study [49], the authors proposed a simplified model where agents communicate through a common field that they generate or utilize to attain an optimal value. Their communication rules ensure that each agent approaches its individual optimum, and the effective three-body interactions make the system highly flexible with numerous pathways to reach the desired state. It should be noted that this model assumes the same optimal field value for all

*aibq@scnu.edu.cn

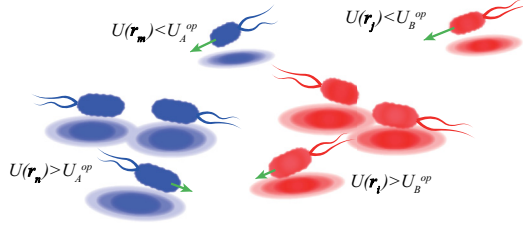


FIG. 1. Schematic illustrating the binary system applicable to our model: type-A particles (blue color) have a target field value of U_A^{op} , while type-B particles (red color) have a target value of U_B^{op} , with both types acting as field sources (represented by blue and red circles) at their respective positions \mathbf{r}_k . The green arrows represent the directional movement of particles with respect to their group members, either moving away from or towards them in order to optimize the field value in their own individual positions.

individuals. However, in real-world scenarios, individuals may have varying optimal values. Therefore, it would be interesting to investigate the impact of heterogeneity in the optimal field on the collective self-optimization of such systems.

To address this issue, we conducted numerical simulation to investigate collective self-optimization of a binary system of communicating active particles with different target field values, based on the findings presented in Ref. [49]. We found that under low-density conditions, both types of particles are able to reach their target field values. However, under medium-density conditions, particles with higher target field values can reach their targets, while particles with lower target field values cannot. Under high-density conditions, both types of particles are unable to reach their target field values. Interestingly, in the process of self-optimization of mixed particles, the mixture can spontaneously separate under certain conditions. Increasing optimal value differences or noise intensity facilitates mixture separation, and there exists an optimal particle number density that maximizes mixture separation. This research contributes to a more in-depth understanding of the collective self-optimization of communication particles and may be valuable in separating species and binary mixtures.

II. MODEL AND METHODS

We consider a model of active particles that communicate through a shared field which they produce or consume, aiming to achieve a specific target field value. Specifically, we study a binary system (as shown in Fig. 1) containing $N/2$ type-A particles (with a target field value of U_A^{op}) and $N/2$ type-B particles (with a target field value of U_B^{op}) in a two-dimensional box of size $L \times L$ with periodic boundary conditions. The active particles attempt to self-optimize their positions \mathbf{r}_i with respect to their target field value U_i^{op} of the collective scalar field $U(\mathbf{r}_i)$ that they self-produce or consume. Depending on the system, U_i^{op} may serve as the optimal oxygen concentration for aerotactic bacteria [29–31], or the comfortable temperature for emperor penguins [40,41].

The scalar field $U(\mathbf{r}_i)$ sensed by particle i at its position \mathbf{r}_i is derived from the three-dimensional diffusion equation (refer to Appendix A for detailed information). It can be expressed as a superposition of single-particle Yukawa orbitals, as

illustrated in the following formula [49]:

$$U(\mathbf{r}_i) = \sum_{j \neq i} Y(|\mathbf{r}_i - \mathbf{r}_j|) = \sum_{j \neq i} C \frac{\exp(-\kappa|\mathbf{r}_i - \mathbf{r}_j|)}{|\mathbf{r}_i - \mathbf{r}_j|}, \quad (1)$$

where κ and C are the scalar field control parameters.

Each particle i is located at position \mathbf{r}_i , and it moves in the direction of $\nabla_i U(\mathbf{r}_i)$ if $U(\mathbf{r}_i) < U_i^{\text{op}}$, and in the opposite direction when $U(\mathbf{r}_i) > U_i^{\text{op}}$. This results in an effective force \mathbf{F}_i acting on particle i [49],

$$\mathbf{F}_i = -\lambda[U(\mathbf{r}_i) - U_i^{\text{op}}]\nabla_i U(\mathbf{r}_i). \quad (2)$$

Here λ represents the alignment strength along the field gradient of each particle i . The primary emphasis of this study lies in the exploration of the realm of heightened heterogeneity within the optimal field value. Typically, under such circumstances, populations exhibit variances in multiple properties, including κ , C , λ , among others. It should be noted that our scope narrows to the specific case of heterogeneity in the optimal field value. Thus, we maintain $\kappa = C = \lambda = 1$ throughout the study.

Considering Eqs. (1) and (2) and defining $r_{i,j} = |\mathbf{r}_i - \mathbf{r}_j|$, the effective force \mathbf{F}_i can be reconstructed as $\mathbf{F}_i = \mathbf{F}_i^p + \mathbf{F}_i^t$. In this equation, $\mathbf{F}_i^p = -\frac{1}{2}\nabla_i \sum_{j \neq i} [Y(r_{i,j}) - U_i^{\text{op}}]^2$ signifies pair interactions, exhibiting Hamiltonian nature. Further, the term $\mathbf{F}_i^t = -\nabla_i [\sum_{j \neq i} \sum_{k \neq i, k > j} Y(r_{i,j})Y(r_{i,k})]$ corresponds to triplet interactions, specifically between particles i , j , and k , and is characterized by a non-Hamiltonian nature. These interactions make the system non-Hamiltonian and highly flexible, enabling particles to achieve their desired state through various collective pathways.

From an microscopic view, the dynamic of each particle i follows the overdamped Langevin equation,

$$\frac{d\mathbf{r}_i}{dt} = \frac{1}{\gamma}\mathbf{F}_i + \boldsymbol{\eta}_i, \quad (3)$$

where γ denotes the friction coefficient. The term $\boldsymbol{\eta}_i$ denotes a zero-mean Gaussian noise with $\langle \boldsymbol{\eta}_i(t)\boldsymbol{\eta}_j(t + \tau) \rangle = 2D_0\delta_{ij}\delta(\tau)\mathbf{I}$. Here \mathbf{I} denotes the unit matrix, and D_0 represents the noise intensity.

According to the mean-field theory, we can determine a critical density, denoted as ρ^* , which is approximately equal to $U^{\text{op}}/2\pi$ (refer to Appendix B for details). Moreover, a solid (uniform) phase is observed at high number densities where $\rho > \rho^*$, thereby hindering the achievement of optimal equilibration. Conversely, for low densities, where $\rho < \rho^*$, we predict a solid-vacuum coexistence (patterned phase), where clusters of particles form with an optimal mean interparticle separation and optimal state. It is crucial to note that the relationship depicted here is also applicable locally. In other words, given the local area meets the requisite conditions, the corresponding uniform and patterned phases materialize locally. For instance, concerning a mixture, when certain conditions are met, a separation of the two types of particles occurs. This results in one form of particle establishing a uniform phase, while the other manifests a patterned phase.

In the case of the mixture, we define $U_A^{\text{op}} = U^{\text{op}} - \delta/2$ and $U_B^{\text{op}} = U^{\text{op}} + \delta/2$, where U^{op} represents the average target field value, and δ represents the difference between the two target fields. The particle number density is defined as

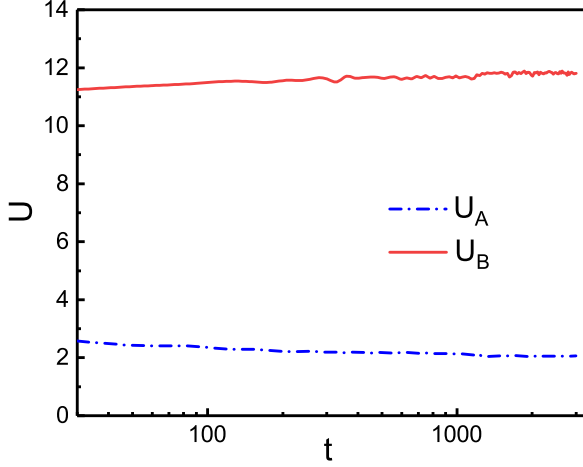


FIG. 2. Time evolution of the field value of type-A (blue) and -B (red) particles at $D_0 = 0.1$, $\delta = 10$, and $\rho = 1.0$.

$\rho = N/L^2$. For convenience in later discussions, we defined the critical density, $\rho^* \approx U^{\text{op}}/2\pi$ for the entire mixed system, $\rho_A^* \approx U_A^{\text{op}}/2\pi$ for type-A particles, and $\rho_B^* \approx U_B^{\text{op}}/2\pi$ for type-B particles.

To quantify the spatial distribution and assess the degree of segregation in our binary mixture, we use the Voronoi tessellation method to define the separation coefficient [15]

$$S = \frac{1}{N} \sum_{i=1}^N 2 \left(\frac{N_i^s}{N_i^t} - \frac{1}{2} \right), \quad (4)$$

where N represents the total number of particles in the system and N_i^s and N_i^t denote the number of similar neighboring particles and all neighboring particles around particle i , respectively. Basing on this definition, $S = 0$ indicates a completely mixed state, while $S = 1$ depicts a completely demixed state.

In our simulations, Eq. (3) were numerically integrated by using a stochastic Runge-Kutta algorithm with the integration step time of 10^{-4} . The computational findings, as depicted in Fig. 2, suggest that once the time exceeds 1000, the mean-field value of the particles primarily stabilizes. With our total integration time exceeding 2000, we ensured the system could reach a nonequilibrium steady state. Particle positions were initialized using a uniform random distribution within the two-dimensional box. We conducted 100 realizations to improve accuracy and minimize statistical errors. Unless otherwise specified, we set $N = 1000$, $\gamma = 1$, and $U^{\text{op}} = 6$. We tested the presented results for robustness against reasonable changes in these parameters.

III. RESULTS AND DISCUSSION

In contrast to previous work where the optimal values pursued by different subjects were equal, our study aims to explore the effects of heterogeneity in optimal values among important explorers on collective self-optimization. Specifically, we investigate to what extent heterogeneity affects collective self-optimization and whether the two types of particles can undergo spontaneous separation, as well as

the conditions for such separation. It is generally known that the segregation of two types of particles must satisfy two conditions: (1) significant differences between the two types of particles leading to disparate motion behaviors and (2) particles of the same type clustering together while those of different types repel each other. This study focuses on two types of particles with different target field values, meeting the first condition. Under appropriate conditions, particles with higher optimal values tend to form larger clusters, while particles with lower optimal values migrate outside of these clusters, meeting the second condition. In the following sections, we investigate the collective self-optimization and segregation dynamics of the binary mixture by varying the noise intensity, particle density, and target difference.

First, we investigate the effect of δ on the collective self-optimization of the binary system at $\rho = 1.0$ and $D_0 = 0.1$. Figures 3(a)–3(d) illustrate the velocity fields of the binary system under varying δ . The particles, rather than being static, exhibit fluctuations attributed to the noise term. Figures 4(a)–4(d) deliver representative snapshots of the binary system under differing δ . Meanwhile, Figs. 4(e)–4(h) provide illustrations of the corresponding mean-field value, $\langle U \rangle$, derived from an average of 100 realizations for each particle. When the two types of particles have identical target field values ($\delta = 0$), they exhibit no difference in their dynamics and mix together. Given that the density $\rho = 1.0$ surpasses the critical density $\rho^* \approx 0.955$, both types particles are in the fluid state as depicted in Fig. 4(a). This implies that both types of particles cannot reach their optimal field values. Consequently, the field values of particles exceed the target field [shown in Fig. 4(e)].

Combined with the preceding paragraph, $\rho^* \approx U^{\text{op}}/2\pi$, $\rho_A^* \approx (U^{\text{op}} - \delta/2)/2\pi$, and $\rho_B^* \approx (U^{\text{op}} + \delta/2)/2\pi$. As a result, when δ increases, ρ_B^* increases, while ρ_A^* decreases. When $\delta > 1.0$, $\rho_A^* < \rho < \rho_B^*$, type-A particles are unable to reach their optimal field value, while type-B particles are able to reach their optimal field value [shown in Figs. 4(f)–4(h)]. When examining a scenario such as $\delta = 3$, considering a context of resource limitation, particle type B, owing to its higher target field value, prioritizes reaching its target field value first. This allows them to achieve optimized interparticle distances and facilitate cluster formation. Type-A particles, on the other hand, are only able to occupy space around clusters formed by type-B particles. Therefore, the two types of particles tend to segregate [shown in Fig. 4(b)]. When the value of δ is sufficiently large (e.g., $\delta = 6$ and 10), the clusters formed by the type-B particles become significantly large, leading to the demixing of the two particle types, as illustrated in Figs. 4(c)–4(d).

It is important to note that the intraparticle spacing differs between particles A and B. This difference is a consequence of the critical density ρ^* , directly affecting the optimal mean interparticle separation, $d^* \propto 1/(\rho^*)^2 \approx 4\pi^2/(U_{\text{op}}^2)$. The optimal mean separation d^* therefore decreases as U_{op} increases. Given that U_B^{op} is greater than U_A^{op} , the optimal mean separation between B particles is smaller than that between A particles. In a situation where spatial resources are insufficient, type-B particles requires less space to reach its target field value than type-A particles. An analysis of the forces

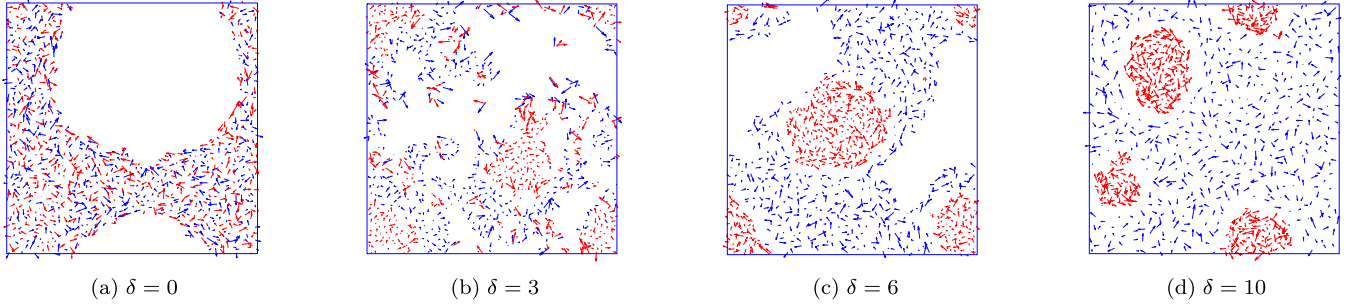


FIG. 3. [(a)–(d)] The velocities of type-A (blue) and -B (red) particles for typical snapshots for different δ at $D_0 = 0.1$ and $\rho = 1.0$. Type-B (red arrows) particles form clusters.

exerted on the particles (as depicted in Fig. 5) reveals a sizable discrepancy in the force experienced by type-B particles, which is considerably larger than that experienced by type-A particles. As a result, type-B particles demonstrate quicker movement, rapid conquest of space, and expedited achievement of their target field values. This suggests that type-B

particles place a priority on promptly attaining their target field.

Figures 4(i) and 4(j) display the average field value, which is independent of time after system equilibrium (shown in Fig. 2), denoted as \bar{U} , and the target value U^{op} of both types of particles, as a function of δ for various D_0 values at $\rho = 1.0$.

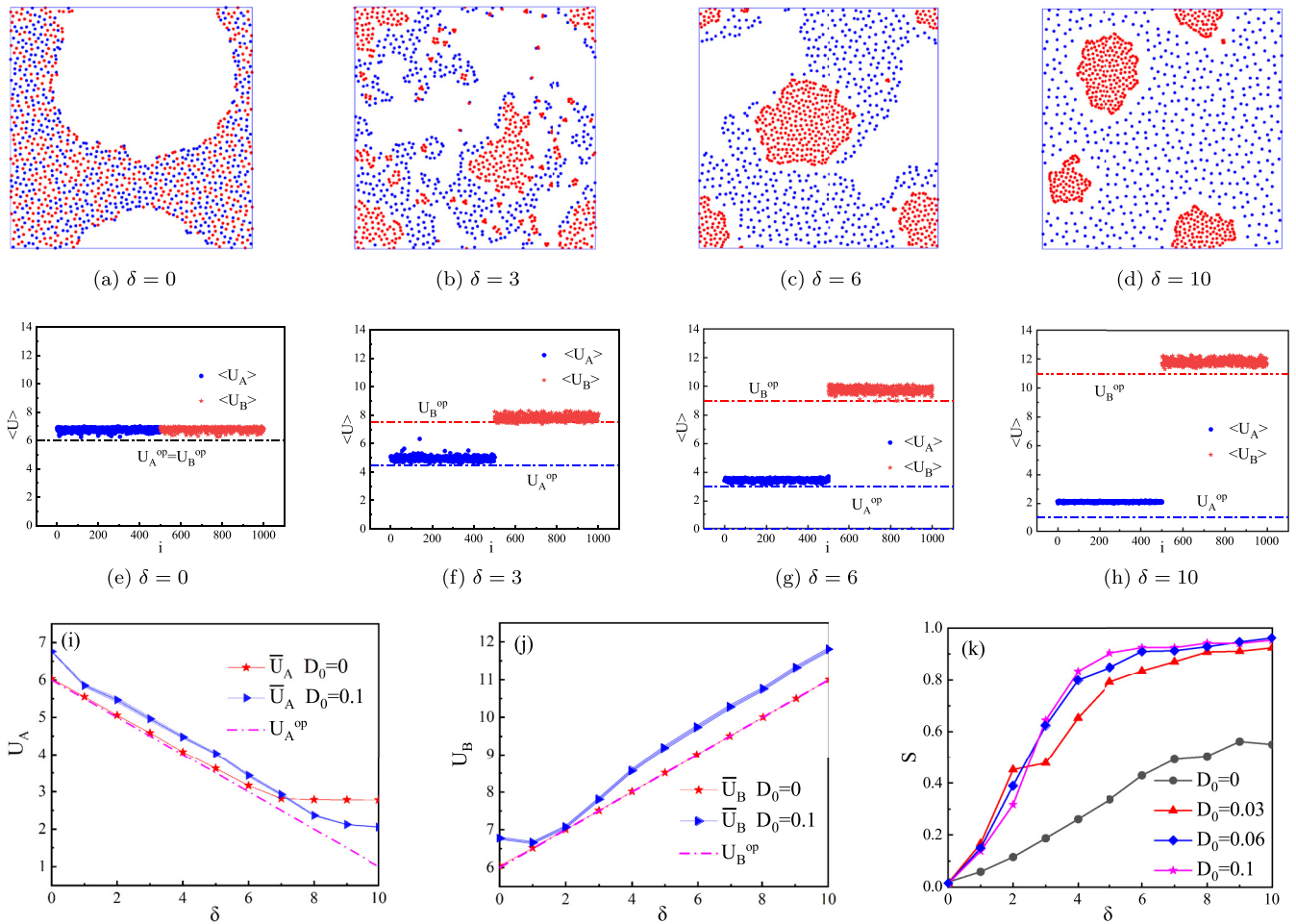


FIG. 4. [(a)–(d)] Typical snapshots of the binary system of 500 type-A particles (blue) and 500 type-B particles (red) for different δ . Type-B (red disks) particles form clusters. [(e)–(h)] The corresponding mean scalar field value $\langle U \rangle$ of each particle, averaged all 100 realizations. Red stars (on the right) represent $\langle U_B \rangle$, while blue dots (on the left) indicate $\langle U_A \rangle$. The dashed lines represent the desired target field value. The other parameters are $\rho = 1.0$ and $D_0 = 0.1$. [(i)–(j)] The average field value and target field value of type-A particles $\bar{U}_A, U_A^{\text{op}}$ (i) and those of type-B particles $\bar{U}_B, U_B^{\text{op}}$ (j) as a function of δ for different D_0 at $\rho = 1.0$. The shaded region shows standard deviation above and below the average. (k) Segregation coefficient S as a function of δ for different D_0 at $\rho = 1.0$.

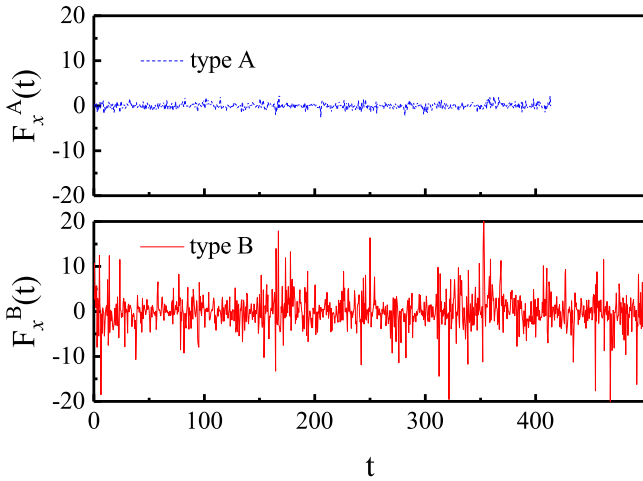


FIG. 5. The figure illustrates the effective force, $F_x(t)$, on particles of type A and type B in the x direction, fluctuating over time, given the parameters $D_0 = 0.1$, $\delta = 10$, and $\rho = 1.0$. The exerted force on type-B particles is significantly higher than that on type-A particles. A comparable trend in forces is also observable in the y direction.

Here the average field value of type-A particles is defined as $\bar{U}_A = \frac{1}{100} \sum_j [\frac{1}{N_A} \sum_i U_{A,i}]_j$, and the sum runs all particles i and realizations j . The same goes for type B particles. When $D_0 = 0$, for low δ ($\delta < 2.0$), type-A particles exhibit an average value that is roughly equal to the target field value. However, as δ increases, the density is moving further and further away from ρ_A^* , \bar{U}_A also gradually diverts from its target field value. When $D_0 = 0.1$, \bar{U}_A remains greater than the optimal value especially when $\delta > 7$. Conversely, with type-B particles, the average value coincides with the target field value when $D_0 = 0$. Since increasing δ on account of the formation of larger clusters, the average field value goes up, which is evident for $D_0 = 0.1$.

Figure 4(k) presents the segregation coefficient S as a function of δ for different D_0 at $\rho = 1.0$. When the particles in the system are identical ($\delta = 0$), two types of particles in system complete mix and S remains 0 irrespective of the noise level. As δ increases, the dynamic discrepancies between the two particle types increase, resulting in a particle segregation and an increase in the S . However, when δ reaches a sufficiently large value ($\delta > 6$), S becomes stable, indicating a steady demixing state. Thus, our binary system could separate when the dynamic difference is significant. From Fig. 4(k), we can also observe the significant role played by noise in the separation of mixtures. For instance, in the absence of noise, separating the mixture can be extremely difficult.

Then, we study the effect of D_0 on the collective self-optimization of the binary system when $\delta = 10$ and $\rho = 1.0$. Figures 6(a)–6(d) display the typical snapshots of our binary system for different values of D_0 , while Figs. 6(e)–6(h) show the mean corresponding field value $\langle U \rangle$ for each particle. Notably, with $\delta = 10$, discernible dynamic differences arise between the two types of particles. Furthermore, when $\rho_A^* < \rho = 1.0 < \rho_B^*$, type-A particles display a uniform state with $U_A > U_A^{\text{op}}$, while type-B particles form clusters and achieve their target field value [shown in Figs. 6(e)–6(h)]. This

conclusion could also be seen in Figs. 6(i) and 6(j), where the average field value of type-B particles can match their target value while that of type-A particles exceed U_A^{op} . When $D_0 = 0$, type-B particles form some small clusters that are surrounded by type-A particles, so the system is mixed [shown in Fig. 6(a)]. Small clusters lacked the energy to break through the surrounding type-A particles to form larger clusters. As D_0 increased, thermal motion enabled the interactions between particles, resulting in small clusters breaking through the surrounding type-A particles to form larger clusters. Appropriately intense noise caused type-B particles to form larger clusters surrounded by type-A particles, eventually leading to mixture segregation [Figs. 6(b)–6(d)]. Therefore, appropriate noise levels facilitated the segregation of the mixture.

Figures 6(i) and 6(j) display the average field value, denoted as \bar{U} and the target value U^{op} of both types of particles, as a function of D_0 for various δ values at $\rho = 1.0$. For low D_0 ($D_0 < 0.01$), the average field value of type-B particles can match their target value while that of type-A particles exceed U_A^{op} . As D_0 increases, \bar{U}_A remains notably far from its target field value, while \bar{U}_B also deviates from its optimal value due to the enlargement of clusters.

The segregation coefficient S for different δ at $\rho = 1.0$ is plotted as a function of D_0 in Fig. 6(k). As previously noted, for $\delta = 0$, the binary system mixed, and S approached 0 regardless of the noise level. However, when the target field value difference increased slightly to $\delta = 3$, S increased with D_0 , but its value remained less than 0.8. For appropriate δ values, such as $\delta = 6$ and 10, an increase in D_0 led to a swift rise in S , which then leveled off as long as noise levels were sufficiently high. These results indicate that under specific conditions, noise can induce mixture segregation. However, if the noise intensity is too high and completely controls the system dynamics, differences between the two particle types will be eradicated, and the system will be completely mixed (not presented in this paper).

The particle number density determines the spatial resources available for the particles to occupy. When the particle density is low, space resources are sufficient, and all particles can achieve their target field values. However, when particle density is high, space resources are limited and the two types of particles need to compete with each other. In this situation, particles with higher target field values will have a priority in reaching the optimal interparticle distance. Next, we will study the impact of the particle density on the collective self-optimization of the binary system at $\delta = 10$ and $D_0 = 0.1$. In this particular case, the values of density are $\rho^* = 0.955$, $\rho_A^* = 0.160$, and $\rho_B^* = 1.750$.

Figures 7(a)–7(d) shows typical snapshots of the binary system for different ρ , while Figs. 7(e)–7(h) demonstrates the corresponding mean-field value $\langle U \rangle$ for each particle. The particle density values can be categorized into three distinct intervals: low density, where $\rho < \rho_A^* < \rho_B^*$; moderate density, where $\rho_A^* < \rho < \rho_B^*$; and high density, where $\rho_A^* < \rho_B^* < \rho$. At low densities (e.g., $\rho = 0.1$) and with abundant spatial resources ($\rho < \rho_A^* < \rho_B^*$), both types of particles can reach their target field values [shown in Fig. 7(e)], forming small clusters individually [see Fig. 7(a)]. As these clusters do not increase in size due to the sufficient space, the mixture remains in a mixed state. As the particle density gradually increases, the

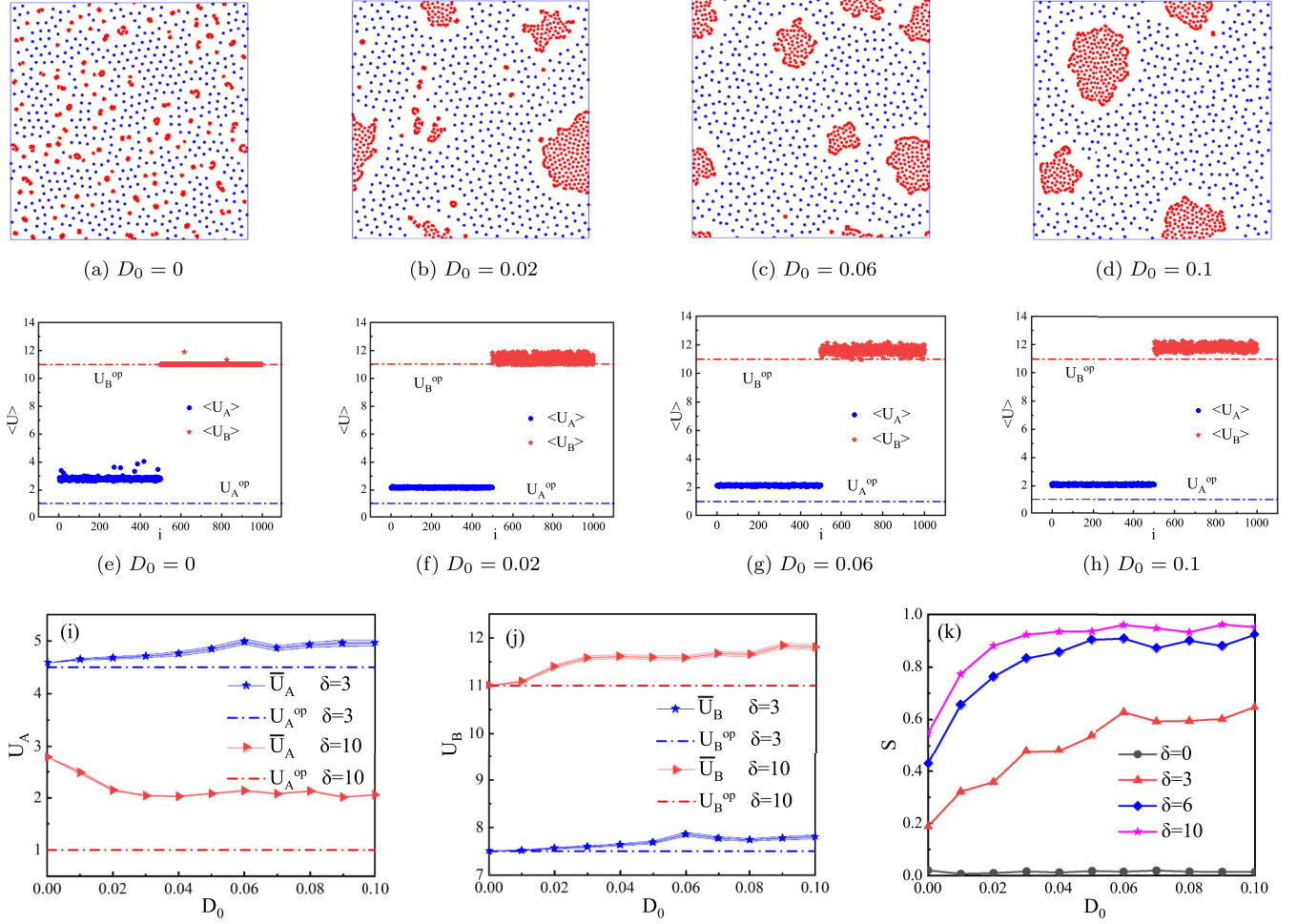


FIG. 6. [(a)–(d)] Typical snapshots of the binary system of 500 type-A particles (blue) and 500 type-B particles (red) for different D_0 . Type-B (red disks) particles form clusters. [(e)–(h)] The corresponding mean scalar field value $\langle U \rangle$ of each particle, averaged all 100 realizations. Red stars (on the right) represent $\langle U_B \rangle$, while blue dots (on the left) indicate $\langle U_A \rangle$. The dashed lines represent the desired target field value. The other parameters are $\rho = 1.0$ and $\delta = 10$. (i) The average field value and target field value of type-A particles \bar{U}_A , U_A^{op} (i) and those of type-B particles \bar{U}_B , U_B^{op} (j) as a function of D_0 for different δ at $\rho = 1.0$. The shaded region shows standard deviation above and below the average. (k) Segregation coefficient S as a function of D_0 for different δ at $\rho = 1.0$.

available space naturally becomes inadequate. When the density of the mixture is between the critical densities of type-A and type-B particles, i.e., $\rho_A^* < \rho < \rho_B^*$ (for instance, $\rho = 0.5$ and 1.0), type-B particles can reach their target field value, while type-A particles cannot [shown in Figs. 7(f)–7(g)]. In this case, type-B particles tend to form larger clusters while type-A particles adopt a fluid state and move around these clusters. This phenomenon allows for the separation of mixtures, as shown in Figs. 7(b)–7(c). When $\rho > \rho_B^* > \rho_A^*$ (e.g., $\rho = 1.9$), neither type of particles can reach their target field value [shown in Fig. 7(h)]. Nonetheless, under the influence of noise, type-B particles still form large clusters, allowing for the separation of the mixture [Fig. 7(d)].

Figures 7(i) and 7(j) display the average field value, denoted as \bar{U} and the target value of both types of particles, as a function of ρ for various D_0 values at $\delta = 10$. In this particular scenario, U_A^{op} is equal to 1 and U_B^{op} is equal to 11, leading to corresponding values of ρ_A^* and ρ_B^* as 0.16 and 1.75,

respectively. In this analysis, we consider the scenario where $D_0 = 0$. For type-B particles ρ perpetually remains less than ρ_B^* . Consequently, type-B particles continuously achieve their optimal field values, resulting in \bar{U}_B and U_B^{op} maintaining consistency. However, for type-A particles, optimal field values are only attainable when ρ is less than 0.16, at which \bar{U}_A and U_A^{op} maintain coherence. Beyond this, as ρ exceeds 0.16, \bar{U}_A diverges from U_A^{op} . Furthermore, a decrease in the average distance between particles leads to an increase in their average field value. With an increase in ρ , the separation between particles decreases, resulting in a corresponding increase in the average \bar{U}_A .

Figure 7(k) depicts the segregation coefficient S as a function of ρ for varying D_0 values at $\delta = 10$. At low densities, the dispersed and small clusters formed by particles blend together, yielding small values of S . As ρ increases from ρ_A^* to ρ_B^* , type-B particles cluster together, while type-A particles remain in a fluid state and move around the clusters. As a

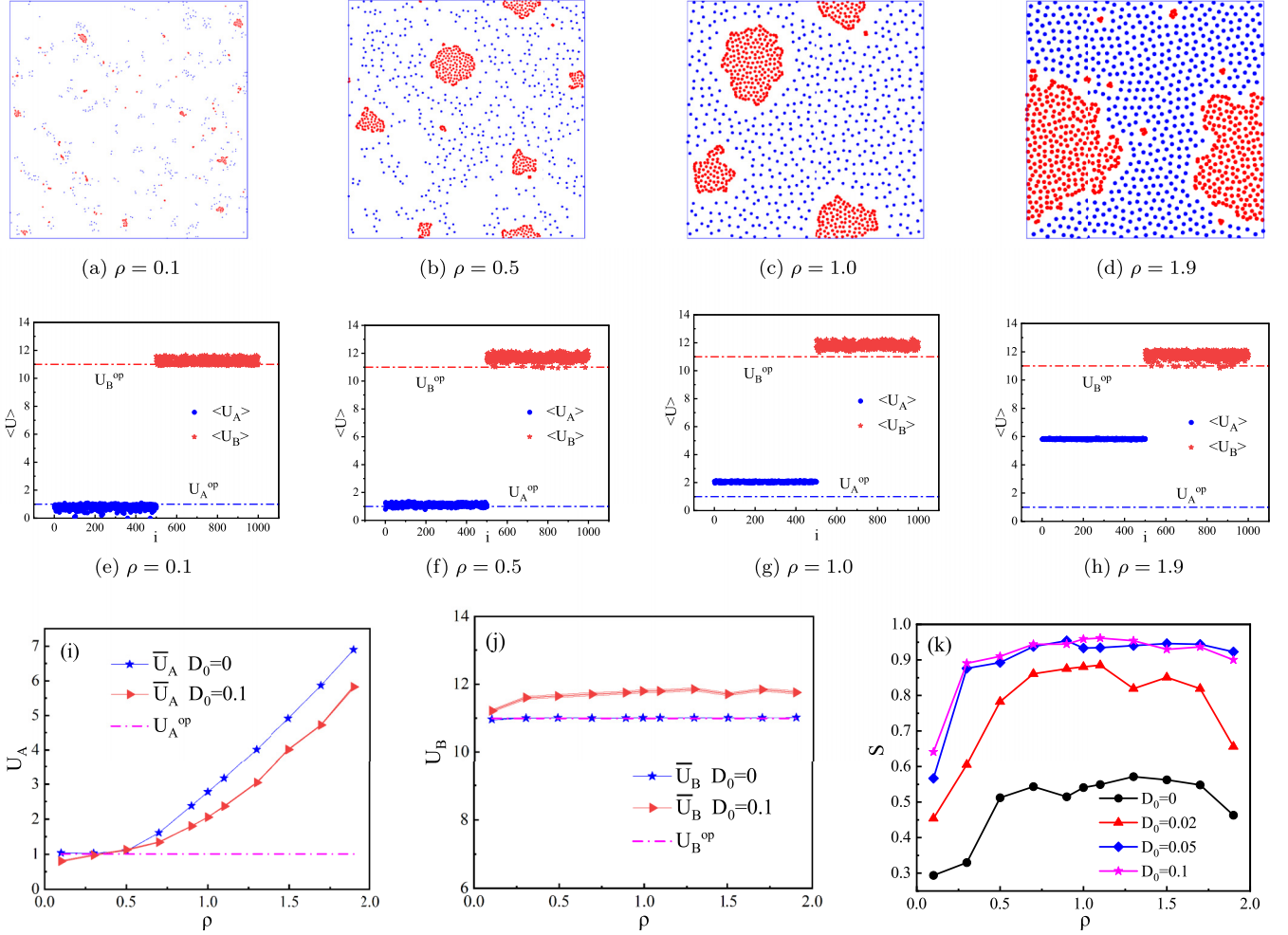


FIG. 7. [(a)–(d)] Typical snapshots of the binary system of 500 type-A particles (blue) and 500 type-B particles (red) for different ρ . Type-B (red disks) particles form clusters. [(e)–(h)] The corresponding mean scalar field value $\langle U \rangle$ of each particle, averaged all 100 realizations. Red stars (on the right) represent $\langle U_B \rangle$, while blue dots (on the left) indicate $\langle U_A \rangle$. The dashed lines represent the desired target field value. The other parameters are $\delta = 10$ and $D_0 = 0.1$. [(i)–(j)] The average field value and target field value of type-A particles \bar{U}_A, U_A^{op} (i) and those of type-B particles \bar{U}_B, U_B^{op} (j) as a function of ρ for different D_0 at $\delta = 10$. The shaded region shows standard deviation above and below the average. As ρ increases, type-A particles gradually divert from optimal state, especially when $D_0 = 0$, while for type-B particles, the average value coincides with the target field value when $D_0 = 0$ and increases on account of the formation of larger clusters when $D_0 = 0.1$. (k) Segregation coefficient S as a function of ρ for different D_0 at $\delta = 10$.

result, the two types of particles separate from each other, and S increases. However, when ρ surpasses both ρ_A^* and ρ_B^* , although the two types of particles can still be separated, the increased interaction between them (resulting in a reduction of the average distance between particles) makes this separation more challenging, leading to a decrease in the segregation coefficient S . Therefore, there exists an optimal particle density at which S is maximal. In addition to previous statements, we herein confirm that noise is a critical factor in the separation of mixtures. For example, even when the density is very high, the mixture cannot be separated in the absence of noise (e.g., $D_0 = 0$).

To further investigate the dependence of the segregation coefficient S , we plot the phase diagrams of the binary mixtures in the $D_0 - \delta$ representation at $\rho = 1.0$ and $D_0 - \rho$ representation at $\delta = 10$ [Figs. 8(a) and 8(b)]. The binary system remains mixed if the target field values of two particles

are identical or the difference between them is insignificant. Additionally, when D_0 is small, the segregation coefficient S is small. When D_0 increases and δ gets large enough, mixture can gradually segregate and the segregation coefficient S increases. Therefore, when the density ρ is fixed, increasing target field value difference and noise intensity facilitates the separation of the mixture [Fig. 8(a)]. When the particle density ρ or noise density D_0 is very low, as mentioned earlier, demixing does not occur and S remains small. As the density ρ increases within appropriate noise intensity, two types of particles are capable of separating, and the segregation coefficient S increases. Therefore, in our model, with a fixed value of δ , the two types of particles can separate when the strength of interactions controlled by the density ρ and noise conditions D_0 , are appropriate [Fig. 8(b)].

Finally, we explore the impact of the system size on the demixing of the mixture, illustrating the relationship

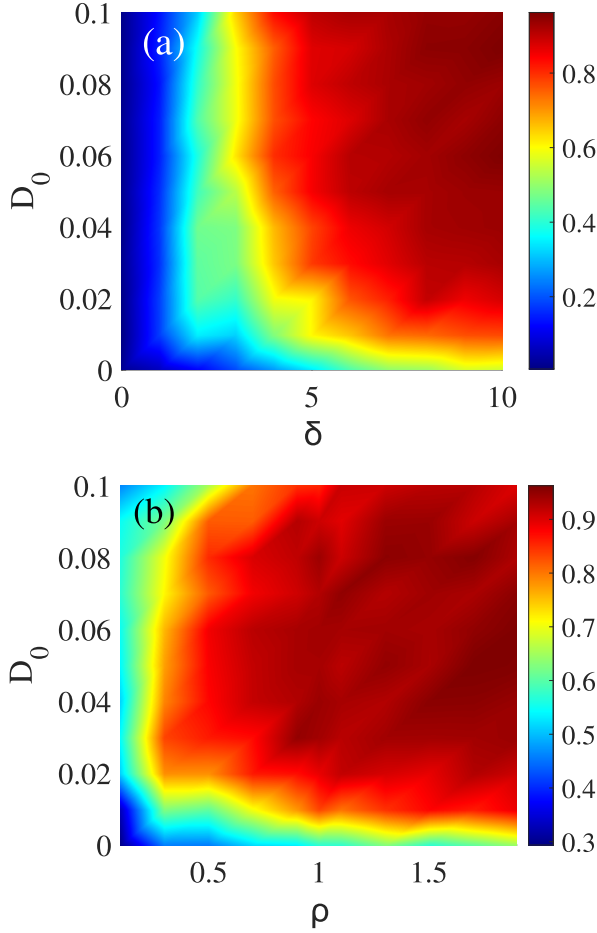


FIG. 8. (a) Phase diagram of the binary mixtures in the $D_0 - \delta$ representation at $\rho = 1.0$. (b) Phase diagram of the binary mixtures in the $D_0 - \rho$ representation at $\delta = 10$. The background represents the value of S according to the color bar on the right.

between the segregation coefficient S and particle number N in Fig. 9. Our findings show an insignificant change in the segregation coefficient S on alteration of the system size N , suggesting that this demixing is unaffected by finite size effects.

Previously, our focus was largely on more pronounced heterogeneities in the optimal field value. We have also explored the impact of less pronounced heterogeneities on the group's ability to reach the optimal state, particularly when demixing is not present as illustrated in Figs. 10(a) and 10(b) at $\rho = 0.5$, $\delta = 1$, and $D_0 = 0.1$. Under conditions of low density and low heterogeneity, the system has sufficient resources, and two types of particles can approach their target field values. However, because the differences in the target field values are too modest, the particles are unable to segregate, resulting instead in the formation of independent, small clusters. Therefore, mixtures with lower heterogeneities are capable of individually achieving their target field values when subjected to lower densities, but they may not necessarily be able to separate. Figure 10(c) illustrates the average field value and the corresponding target field value as a function of ρ at $\delta = 1$ and $D_0 = 0.1$. Despite the apparent differences in target field values, the conditions whereby each particle attains its

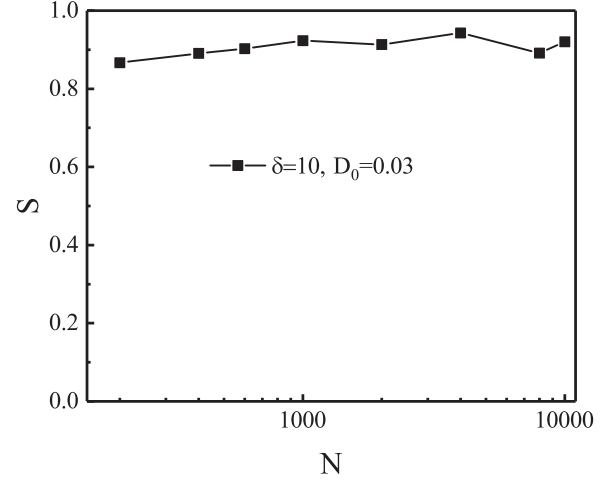


FIG. 9. Segregation coefficient S as a function of particle number N at $\rho = 1.0$, $\delta = 10$, and $D_0 = 0.03$. We illustrate the nonexistence of finite size effects, demonstrating that the segregation coefficient S can be achieved regardless of the system size N .

individual target field value are consistently independent. This is conditional on the premise that $\rho < U_{A(B)}^{\text{op}}/2\pi$.

IV. CONCLUSION AND OUTLOOK

In this study, we have investigated the collective self-optimization and segregation dynamics of a binary system comprising communicating active particles with different target field values by varying the noise intensity, particle density, and target value difference. Our main focus was to determine how heterogeneity in optimal field affects the collective self-optimization in such a system. We found that under low-density conditions, both types of particles were able to reach their target field values. However, under medium-density conditions, particles with higher target field values could reach their targets, while particles with lower target field values could not. Under high-density conditions, both types of particles were unable to reach their target field values. Interestingly, we also observed that in the process of self-optimization, the mixture of particles could spontaneously separate under certain conditions. Suitable noise intensity, particle density, and significant differences in optimal values for both types of particles were necessary for the separation of the mixture. Increasing the optimal value differences or noise intensity facilitated mixture separation, and there exists an optimal particle number density that maximizes mixture separation.

In order to maximize the chances of the survival of members in a social group, collective self-organization must strike an optimal balance between maximizing individual interests and enhancing collective welfare to the highest possible extent. Therefore, it is necessary to investigate how multiple populations can achieve this balance under conditions of limited resources. Our study reveals that during the self-optimization process of multiple population entities, similar entities will naturally cluster together and separate from one another to maximize their respective benefits. These

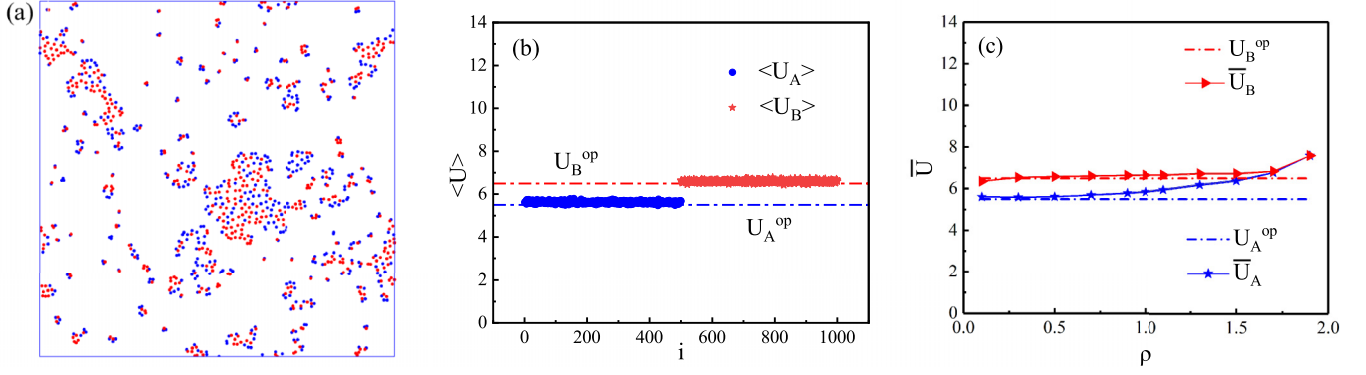


FIG. 10. (a) Typical snapshots of the binary system of 500 type-A particles (blue) and 500 type-B particles (red) at $\rho = 0.5$, $\delta = 1$, and $D_0 = 0.1$. (b) The corresponding mean scalar field value $\langle U \rangle$ of each particle, averaged all 100 realizations. Red stars (on the right) represent $\langle U_B \rangle$, while blue dots (on the left) indicate $\langle U_A \rangle$. The dashed lines represent the desired target field value. (c) The average field value and the corresponding target field value as a function of ρ at $\delta = 1$ and $D_0 = 0.1$.

findings can aid in the optimization of the aggregation of multiple active agents within populations, or help to identify communication protocols that certain social groups employ to maximize their likelihood of survival. Furthermore, the task of segregating mixed active particles is of utmost importance [1–20], thus our findings are pertinent to gaining valuable insights into this process.

Heterogeneity is a universal characteristic observed in all natural systems at various scales, hence our model has considerable practical applicability. For instance, under specific oxygen conditions, two different types of aerotactic bacteria [37] coexist, each with distinct optimal oxygen concentration requirements. Similarly, within a defined space, diverse types of penguins (either different species, or adults and juveniles of the same species) maintain individual optimum temperature preferences for comfort [41]. In addition, in the context of heterogeneous populations, sophisticated mechanisms, such as differentiation of roles into leaders and followers [50], are often necessary to foster cooperation among individuals. The different types of particles in these examples can respectively be viewed as type-A and type-B particles in our model.

Our work primarily focuses on two dimensions. However, previous research [51–55] has demonstrated intriguing aggregation patterns in cases involving Morse potentials across both two and three dimensions. Consequently, extending our work to three dimensions and exploring three-dimensional patterns would be a meaningful endeavor. Furthermore, considering the nonreciprocal interactions between different types of mixtures and studying how nonreciprocity affects the collective dynamics of the group is also of great interest.

ACKNOWLEDGMENTS

This work was supported in part by the National Natural Science Foundation of China (Grant No. 12075090), the Guangdong basic and applied basic research foundation (Grants No. 2022A1515010449 and No. 2022A1515110250), and Science and Technology Projects in Guangzhou (Grant No. 2023A04J0042).

APPENDIX A: THE SCALAR FIELD $U(\mathbf{r}_i)$

We assume that the evolution of the scalar field is governed by the three-dimensional diffusion equation [49]

$$\frac{\partial U_{3D}}{\partial t} = D\nabla^2 U_{3D} - k_d U_{3D} - k_s \sum_j \delta(\mathbf{r} - \mathbf{r}_j), \quad (\text{A1})$$

where D is the diffusion constant of the field, k_d represents the loss rate attributed to potential external factors, and k_s represents the emission rate of each particle source. The sum is taken over all particle indices j . In many instances, the chemical dynamics occur at a rapid pace compared to other relevant timescales within a given system (e.g., the response time of a microorganism). In such cases, our primary interest lies in the steady-state profile, which corresponds to $\frac{\partial U_{3D}}{\partial t} = 0$ in the Eq. (A1). The steady-state solution, $U_{3D}(\mathbf{r})$, can be represented as a superposition of single-particle Yukawa orbitals, as shown in the following formula:

$$U_{3D}(\mathbf{r}) = \sum_j Y(|\mathbf{r} - \mathbf{r}_j|) = \sum_j C \frac{\exp(-\kappa|\mathbf{r} - \mathbf{r}_j|)}{|\mathbf{r} - \mathbf{r}_j|}, \quad (\text{A2})$$

where $C = k_s/(4\pi D)$ and $\kappa = \sqrt{k_d/D}$.

Note that the particles in our system are confined to a two-dimensional xy plane. We define the scalar field $U(x, y) = U_{3D}(x, y, 0)$ for two dimensions. Therefore, the two-dimensional stationary field $U(\mathbf{r})$ has the same form as the three-dimensional field, except that in the three-dimensional equations, the z coordinate is set to zero.

$$U(\mathbf{r}) = \sum_j Y(|\mathbf{r} - \mathbf{r}_j|) = \sum_j C \frac{\exp(-\kappa|\mathbf{r} - \mathbf{r}_j|)}{|\mathbf{r} - \mathbf{r}_j|}. \quad (\text{A3})$$

In the two-dimensional xy plane, the field sensed by particle i at its position \mathbf{r}_i can be expressed as $U(\mathbf{r}_i) = \sum_{j \neq i} Y(|\mathbf{r}_i - \mathbf{r}_j|)$, with the self-interaction being ignored. Hence, we obtain Eq. (1), which is presented in the main text.

APPENDIX B: THE CRITICAL DENSITY FROM MEAN-FIELD THEORY

Following the steps outlined in Ref. [49], we now derive the approximate critical density using mean-field theory at $\kappa = C = \lambda = \gamma = 1$. To address the coupled three-dimensional field equation and two-dimensional density equation, we introduce two distinct types of quantities: the three-dimensional variables $U_{3D}(x, y, z, t)$ and $\rho_{3D}(x, y, z, t)$, along with their two-dimensional counterparts $U(x, y, t)$ and $\rho(x, y, t)$. In the context of our model, where particles are confined to movement on the two-dimensional xy plane, it follows that $\rho_{3D}(x, y, z, t) = \rho(x, y, t)\delta(z)$ and $U(x, y, t) = U_{3D}(x, y, 0, t)$.

In the context of continuum theories, Eq. (A1) can be expressed in the following form through nondimensionalization:

$$\frac{\partial U_{3D}}{\partial t} = \frac{1}{4\pi} \nabla^2 U_{3D} - \frac{1}{4\pi} U_{3D} + \rho_{3D}. \quad (\text{B1})$$

From Eq. (3), we can derive the corresponding Fokker-Planck equation [56], which governs the two-dimensional density $\rho(x, y, t)$,

$$\frac{\partial \rho}{\partial t} = \nabla[\rho(U - U^{\text{op}})\nabla U] + D_0 \nabla^2 \rho. \quad (\text{B2})$$

By assuming a constant density $\bar{\rho}$ within the two-dimensional plane and substituting $\rho_{3D} = \bar{\rho}\delta(z)$ into Eq. (B1), we obtain the static solution for the coupled equations [Eqs. (B1) and (B2)],

$$\rho = \bar{\rho}, \quad U_{3D} = 2\pi\bar{\rho} \exp(-|z|). \quad (\text{B3})$$

This solution represents the solid or uniform phase.

A linear stability analysis is conducted around the homogeneous equilibrium as denoted in Eq. (B3). To examine the linear stability of the steady state to spatially inhomogeneous perturbations, we assume $\rho = \bar{\rho} + \tilde{\rho} \exp(ikr - \sigma t)$ and $\rho_{3D} = 2\pi\bar{\rho} \exp(-|z|) + \tilde{u}(z) \exp(ikr - \sigma t)$, where $\tilde{\rho}$ and $\tilde{u}(z)$ are very small quantities. By substituting this ansatz into Eqs. (B1) and (B2) and neglecting higher-order infinitesimal terms, we obtain a system of linear equations in terms of $\tilde{\rho}$ and $\tilde{u}(z)$. Analyzing the conditions for the solvability of this system of linear equations reveals that stability is achieved when the following condition is satisfied:

$$\bar{\rho} \geq \frac{U^{\text{op}} + \sqrt{(U^{\text{op}})^2 - 4D_0}}{4\pi}. \quad (\text{B4})$$

Consequently, in situations with zero noise ($D_0 = 0$), the homogeneous solid phase demonstrates stability if $\bar{\rho} \geq U^{\text{op}}/(2\pi)$, and instability when the contrary is true.

-
- [1] M. Mijalkov and G. Volpe, *Soft Matter* **9**, 6376 (2013).
- [2] N. H. P. Nguyen, D. Klotsa, M. Engel, and S. C. Glotzer, *Phys. Rev. Lett.* **112**, 075701 (2014).
- [3] I. Berdakin, Y. Jeyaram, V. V. Moshchalkov, L. Venken, S. Dierckx, S. J. Vanderleyden, A. V. Silhanek, C. A. Condat, and V. I. Marconi, *Phys. Rev. E* **87**, 052702 (2013).
- [4] S. N. Weber, C. A. Weber, and E. Frey, *Phys. Rev. Lett.* **116**, 058301 (2016).
- [5] S. Kumari, A. S. Nunes, N. A. M. Araujo, and M. M. T. Gama, *J. Chem. Phys.* **147**, 174702 (2017).
- [6] C. Reichhardt and C. J. Olson Reichhardt, *Phys. Rev. E* **88**, 042306 (2013).
- [7] S. R. McCandlish, A. Baskarana, and M. F. Hagan, *Soft Matter* **8**, 2527 (2012).
- [8] J. Stenhammar, R. Wittkowski, D. Marenduzzo, and M. E. Cates, *Phys. Rev. Lett.* **114**, 018301 (2015).
- [9] J. Smrek and K. Kremer, *Phys. Rev. Lett.* **118**, 098002 (2017).
- [10] J. Harder and A. Cacciuto, *Phys. Rev. E* **97**, 022603 (2018).
- [11] A. Costanzo, J. Elgeti, T. Auth, G. Gompper, and M. Ripoll, *Europhys. Lett.* **107**, 36003 (2014).
- [12] A. Nourhani, V. H. Crespi, and P. E. Lammert, *Phys. Rev. Lett.* **115**, 118101 (2015).
- [13] A. Agrawal and S. B. Babu, *Phys. Rev. E* **97**, 020401(R) (2018).
- [14] D. Levis and B. Liebchen, *Phys. Rev. E* **100**, 012406 (2019).
- [15] P. Sahu, D. M. Sussman, M. RübSam, A. F. Mertz, V. Horsley, E. R. Dufresne, C. M. Niessen, M. C. Marchetti, M. L. Manning, and J. M. Schwarz, *Soft Matter* **16**, 3325 (2020).
- [16] B. Q. Ai and R. X. Guo, *Phys. Rev. E* **104**, 064411 (2021).
- [17] T. Barois, J. F. Boudet, J. S. Lintuvuori, and H. Kellay, *Phys. Rev. Lett.* **125**, 238003 (2020).
- [18] D. Levis, I. Pagonabarraga, and B. Liebchen, *Phys. Rev. Res.* **1**, 023026 (2019).
- [19] C. Scholz, M. Engel, and T. Pöschel, *Nat. Commun.* **9**, 931 (2018).
- [20] A. Geiseler, P. Hänggi, F. Marchesoni, C. Mulhern, and S. Savel'ev, *Phys. Rev. E* **94**, 012613 (2016).
- [21] C. M. Waters and B. L. Bassler, *Annu. Rev. Cell Dev. Biol.* **21**, 319 (2005).
- [22] A. Ziepke, I. Maryshev, I. S. Aranson, and E. Frey, *Nat. Commun.* **13**, 6727 (2022).
- [23] G. H. Wadhams and J. P. Armitage, *Nat. Rev. Mol. Cell Biol.* **5**, 1024 (2004).
- [24] M. Eisenbach, *J. Cell. Physiol.* **213**, 574 (2007).
- [25] M. Kollmann, L. Løvdok, K. Bartholomé, J. Timmer, and V. Sourjik, *Nature (Lond.)* **438**, 504 (2005).
- [26] U. B. Kaupp, N. D. Kashikar, and I. Weyand, *Annu. Rev. Physiol.* **70**, 93 (2008).
- [27] C. Hoell and H. Löwen, *Phys. Rev. E* **84**, 042903 (2011).
- [28] A. Sengupta, S. van Teeffelen, and H. Löwen, *Phys. Rev. E* **80**, 031122 (2009).
- [29] B. L. Taylor, *Trends Biochem. Sci.* **8**, 438 (1983).
- [30] B. L. Taylor, I. B. Zhulin, and M. S. Johnson, *Annu. Rev. Microbiol.* **53**, 103 (1999).
- [31] I. B. Zhulin, V. A. Beshpalov, M. S. Johnson, and B. L. Taylor, *J. Bacteriol.* **178**, 5199 (1996).
- [32] B. Ramm, A. Goychuk, A. Khmelinskaia, P. Blumhardt, H. Eto, K. A. Ganzinger, E. Frey, and P. Schwille, *Nat. Phys.* **17**, 850 (2021).
- [33] D. Gorbonos, R. Ianculescu, J. G. Puckett, R. Ni, N. T. Ouellette, and N. S. Gov, *New J. Phys.* **18**, 073042 (2016).

- [34] R. K. Katzschmann, J. DelPreto, R. MacCurdy, and D. Rus, *Sci. Rob.* **3**, eaar3449 (2018).
- [35] S. G. Li, R. Batra, D. Brown, H. D. Chang, N. Ranganathan, C. Hoberman, D. Rus, and H. Lipson, *Nature (Lond.)* **567**, 361 (2019).
- [36] B. C. Mazzag, I. B. Zhulin, and A. Mogilner, *Biophys. J.* **85**, 3558 (2003).
- [37] M. Elmas, V. Alexiades, L. Ó'Neal, and G. Alexandre, *BMC Microbiol.* **19**, 101 (2019).
- [38] T. K. Douglas, C. E. Cooper, and P. C. Withers, *J. Exp. Biol.* **220**, 1341 (2017).
- [39] C. J. Gordon, *Phys. Behav.* **47**, 963 (1990).
- [40] C. Gilbert, S. Blanc, Y. Le Maho, and A. Ancel, *J. Exp. Biol.* **211**, 1 (2008).
- [41] A. Ancel, H. Visser, Y. Handrich, D. Masman, Y. Le Maho, *Nature (Lond.)* **385**, 304 (1997).
- [42] K. J. Painter, *J. Theor. Biol.* **481**, 162 (2019).
- [43] E. J. Marsden, C. Valeriani, I. Sullivan, M. E. Cates, and D. Marenduzzo, *Soft Matter* **10**, 157 (2014).
- [44] E. F. Keller and L. A. Segel, *J. Theor. Biol.* **30**, 225 (1971).
- [45] T. Hillen and K. J. Painter, *J. Math. Biol.* **58**, 183 (2009).
- [46] T. Hillen and K. Painter, *Adv. Appl. Math.* **26**, 280 (2001).
- [47] K. J. Painter and T. Hillen, *Can. Appl. Math. Q.* **10**, 501 (2002).
- [48] D. Wrzosek, *Math. Model. Nat. Phenom.* **5**, 123 (2010).
- [49] A. V. Zampetaki, B. Liebchen, A. V. Ivlev, and H. Löwen, *Proc. Natl. Acad. Sci. USA* **118**, e2111142118 (2021).
- [50] D. Pais and N. E. Leonard, *Physica D* **267**, 81 (2014).
- [51] M. R. D'Orsogna, Y. L. Chuang, A. L. Bertozzi, and L. S. Chayes, *Phys. Rev. Lett.* **96**, 104302 (2006).
- [52] Y. L. Chuang, M. R. D'Orsogna, D. Marthaler, A. L. Bertozzi, and L. S. Chayes, *Physica D* **232**, 33 (2007).
- [53] A. J. Leverentz, C. M. Topaz, and A. J. Bernoff, *SIAM J. Appl. Dyn. Syst.* **8**, 880 (2009).
- [54] N. H. P. Nguyen, E. Jankowski, and S. C. Glotzer, *Phys. Rev. E* **86**, 011136 (2012).
- [55] Y. L. Chuang, T. Chou, and M. R. D'Orsogna, *Phys. Rev. E* **93**, 043112 (2016).
- [56] H. Risken, *The Fokker-Planck Equation*, 2nd ed. (Springer-Verlag, Berlin, 1989)